Exceptional-surface-enhanced rotation sensing with robustness in a whispering-gallery-mode microresonator

Wenxiu Li,[1] Yang Zhou,[2] Peng Han,[1] Xiaoyang Chang,[1] Shuo Jiang,[1] Anping Huang,[1] Hao Zhang,[2,*] and Zhisong Xiao[1]

[1]*School of Physics, Beihang University, Beijing 100191, China*

[2]*Research Institute of Frontier Science, Beihang University, Beijing 100191, China*

(Received 5 March 2021; accepted 18 August 2021; published 7 September 2021)

Traditional optical gyroscopes rely on the Sagnac effect that the resonant frequency shift is linear with the rotation rate. Recently, optical gyroscopes operating near an exceptional point (EP) have been extensively investigated to improve the response to rotation. However, the high-performance implementation of this kind of gyroscope requires strict conditions, which restrict the practical application of these devices. In this paper, a non-Hermitian photonic configuration based on a single resonator is proposed to establish an exceptional surface (EP surface) constructed of numerous EPs. It is demonstrated theoretically that rotation-induced frequency splitting in our configuration is four orders of magnitude higher than that in the traditional gyroscope. We also investigate the shot-noise-limited minimum detectable rotation rate compared to the conventional gyroscope with the same radius and intrinsic loss, when the system is tuned around the EP. This proposed approach attempts to combine robustness with high sensitivity detection of the rotation.

DOI: 10.1103/PhysRevA.104.033505

I. INTRODUCTION

Resonant optical gyroscopes are based on the Sagnac effect, namely, the resonant frequency difference of the counterpropagating traveling waves [clockwise (CW) and counterclockwise (CCW) waves] in a rotating resonator is linear with the rotation rate Ω [1–4]. Recently, non-Hermitian optical gyroscopes operating near an exceptional point (EP) exhibited excellent performances in rotation detection [5–10]. In quantum open systems, EPs are non-Hermitian degeneracies, at which the eigenvalues degenerate and the corresponding eigenmodes coalesce. They have been extended to various non-Hermitian optical systems via parity-time ($\mathcal{PT}$) symmetry [11–20], anti-$\mathcal{PT}$ symmetry [21–24], and optical chiral behaviors [25–29].

According to the above concepts, different versions of optical gyroscopes based on EPs have been designed to enhance rotation detection in theory and experiments. The $\mathcal{PT}$-symmetric ring laser gyroscope (RLG) and anti-$\mathcal{PT}$-symmetric gyroscope operating at an EP result in sensitivity several orders of magnitude higher than that of classical gyroscopes [5,6]. An experimental version of the non-Hermitian Brillouin laser gyroscope has been successfully built in a resonator in which the predicted EP-enhanced Sagnac effect was generated to obtain a fourfold enhancement of the scale factor [8]. In the same period, Lai *et al.* judiciously modified a commercial helium-neon RLG to operate it at an EP [9]. The response of this device shows a square-root dependence on the rotational speed and the sensitivity is enhanced up to 20 times compared to the commercial RLG.

Despite the tremendous advantage of EP sensors in sensitivity enhancement, most of them suffer from the fabrication errors or experimental uncertainties. In practice, the strong response of the EP-based sensors generally requires strict implementation conditions of simultaneous and precise controlling parameters. As a result, EP-based sensors are very susceptible to external errors and the actual sensitivities of these devices fall short of theoretical expectations.

Recently, the notion of the EP surface was presented and a corresponding configuration to implement it was designed to overcome the challenges faced by EP-based sensors [30,31]. In comparison with an isolated EP, an EP surface constructed of numerous EPs provides additional degrees of freedom that can make the working point shift along the EP surface when the system experiences undesired perturbations. Such an arrangement has been demonstrated to be robust against external perturbations [31]. In previous works, the EP surface was constructed of a specific type of EP, called chiral EP, which arises from the unbalanced contribution of CW and CCW traveling modes in a whispering-gallery-mode (WGM) resonator. However, this kind of chiral EP is not appropriate for detecting rotation because the rotation of a resonator cannot produce additional coupling between CW and CCW modes.

In this paper, we present a non-Hermitian photonic configuration in order to establish an EP surface constructed of numerous chiral EPs. A mechanism is introduced to enhance the rotation detection using the chiral EP. We demonstrate theoretically that the enhanced frequency splitting and noise-limited precision of our configuration operate around the EP. This scheme can be exploited to combine robustness with enhanced sensitivity of the rotation detection.

II. ENHANCEMENT OF ROTATION SENSING AT A CHIRAL EP

In a WGM microresonator, the asymmetric backscattering between counterpropagating optical modes is related to

*haozhang@buaa.edu.cn

the chiral EPs. At a chiral EP, CW and CCW traveling modes coalesce into one mode owing to a fully asymmetric backscattering between the counterpropagating modes. With the coupled-mode theory, this feature can be well described by a non-Hermitian Hamiltonian H_0 [27,31],

$$i\frac{d}{dt}\begin{bmatrix} a_{\rm CW} \\ a_{\rm CCW} \end{bmatrix} = H_0 \begin{bmatrix} a_{\rm CW} \\ a_{\rm CCW} \end{bmatrix}, \quad H_0 = \begin{bmatrix} \omega_0 - i\gamma & 0 \\ A_0 & \omega_0 - i\gamma \end{bmatrix}, \tag{1}$$

where $a_{\rm CW}$ and $a_{\rm CCW}$ are the intracavity mode fields in the CW and CCW directions, respectively; ω_0 is the resonance frequency; γ denotes the effective loss or gain coefficient, i.e., $\gamma = \gamma_0 + \kappa/2 - g$, where γ_0 is the intrinsic loss rate, κ is the external coupling rate, and g is the external gain rate; and A_0 quantifies the intrinsic backscattering strength. The complex eigenvalues of H_0 are $\omega_{\rm EP1,2} = \omega_0 - i\gamma$ and the corresponding eigenvectors coalesce to one vector $\tilde{a}_{1,2} = (0, 1)^T$. In this case, the resonator supports a pair of degenerate cavity modes with identical resonance frequency ω_0.

When a resonator rotates with a rate of Ω (in the CCW direction), CW and CCW modes experience an opposite Sagnac frequency shift that can be described by the perturbed Hamiltonian $H_I = \left[\begin{smallmatrix} \Delta\omega_s & 0 \\ 0 & -\Delta\omega_s \end{smallmatrix}\right]$. The Sagnac shift is $\Delta\omega_s = 4\pi R\Omega/n_g\lambda$, where R is the resonator radius, n_g is the group index, and λ is the operating wavelength. In a conventional resonator operating at a diabolic point (DP) [32], the rotation-induced frequency splitting between the two counterpropagating modes is $\Delta\omega_{\rm DP} = 2\Delta\omega_s$. Once the system operating at a chiral EP is subject to rotation, the perturbed system is described by an effective non-Hermitian matrix

$$H = H_0 + H_I = \begin{bmatrix} \omega_0 + \Delta\omega_s - i\gamma & 0 \\ A_0 & \omega_0 - \Delta\omega_s - i\gamma \end{bmatrix}. \tag{2}$$

Now the eigenvalues of the total Hamiltonian H are $\omega_{\rm EP1,2} = \omega_0 - i\gamma \pm \Delta\omega_s$. It should be noted that the corresponding mode splitting $\Delta\omega_{\rm EP} = 2\Delta\omega_s$ shows distinctly a linear dependence on the rotation rate. The square-root response to rotation does not occur at a chiral EP [5,6]. Hence, to enhance the rotation detection using a chiral EP, we need to construct a new perturbed form induced by rotation as

$$H_{\rm ind} = \begin{bmatrix} \Delta\omega_s & B_1(\Delta\omega_s) \\ 0 & -\Delta\omega_s \end{bmatrix}, \tag{3}$$

where the backscattering coefficient $B_1(\Delta\omega_s)$ is related to the rotation. The Hamiltonian $H_{\rm ind}$ shows that the rotation not only induces the Sagnac shift but also results in the mode coupling between the CW and CCW modes. The total Hamiltonian is $H = H_0 + H_{\rm ind}$ and the resulting eigenfrequencies of H are

$$\omega_{\pm} = \omega_0 - i\gamma \pm \sqrt{B_1(\Delta\omega_s)A_0 + \Delta\omega_s^2}. \tag{4}$$

Equation (4) demonstrates that the rotation-induced perturbation forces the system to depart from the EP, triggering an eigenfrequency splitting. The complex eigenfrequency splitting is calculated as

$$\Delta\omega_{\rm EP} = \omega_+ - \omega_- = 2\sqrt{B_1(\Delta\omega_s)A_0 + \Delta\omega_s^2}. \tag{5}$$

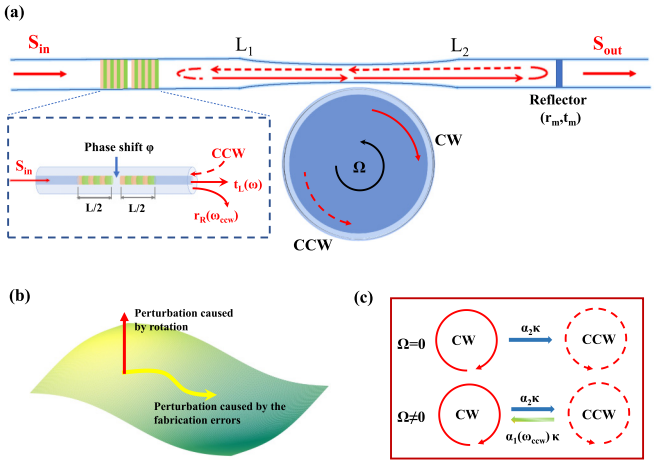

FIG. 1. (a) Schematic of a non-Hermitian photonic structure. A WGM microresonator is coupled to a fiber taper with a reflector on one side and a phase-shifted FBG on the other side. The blue (dashed line) box shows a schematic of a phase-shift FBG. At the phase-shifted FBG, the left-incident signal is $S_{\rm in}$ and the right-incident signal is the CCW mode. (b) Schematic diagram of an EP surface [31]. The EP surface exhibits the characteristic that the operating point of the system will shift along the surface when it experiences undesired perturbations. (c) Optical mode-coupling situations in the absence or presence of the rotation. The CW and CCW optical modes in the WGM microresonator are represented by red solid and dotted circles, respectively.

Assuming a sufficiently small rotation, i.e., $\Delta\omega_s \ll B_1 \ll A_0$, the complex eigenfrequency splitting $\Delta\omega_{\rm EP} \approx 2\sqrt{B_1(\Delta\omega_s)A_0}$, which shows that the frequency splitting has a square-root dependence on $B_1(\Delta\omega_s)$. That is the characteristic of EP sensing. This result clearly indicates that the perturbation form presented in Eq. (3) provides a mechanism to enhance rotation detection using a chiral EP. The enhancement factor S_e defined by the ratio of $\Delta\omega_{\rm EP}$ to $\Delta\omega_{\rm DP}$ is

$$S_e = \frac{\Delta\omega_{\rm EP}}{\Delta\omega_{\rm DP}} = \frac{\sqrt{B_1(\Delta\omega_s)A_0}}{\Delta\omega_s}, \tag{6}$$

which is therefore proportional to $\sqrt{A_0 B_1}$ and inversely proportional to the Sagnac shift $\Delta\omega_s$. From Eq. (6) we see that the larger A_0 is required and the perturbation B_1 needs to dramatically increase with the Sagnac shift $\Delta\omega_s$ to enhance the frequency splitting.

III. NON-HERMITIAN EP SURFACE SYSTEM FOR ENHANCING ROTATION DETECTION

In this section, we present a way to establish an EP surface with a single resonator. Compared with the $\mathcal{PT}$-symmetric and anti-$\mathcal{PT}$-symmetric coupled resonators [5,6], a single resonator is applied more flexibly in practice. This non-Hermitian photonic system is shown in Fig. 1(a), where a WGM resonator is coupled to a fiber taper with a coupling rate κ. In the absence of rotation, the microresonator supports two counterpropagating WGM modes with the same resonance frequency ω_0. A phase-shifted fiber Bragg grating (FBG) is introduced on one end of the fiber with a reflectivity $r_R(\omega_{\rm CCW})$.

In addition, a partial reflector with reflectivity r_m is on the other side of the fiber.

Due to the presence of the reflector and the phase-shifted FBG, the counterpropagating WGM modes are coupled with each other. The dynamics of the system can be described by the coupled-mode equations as [25,28]

$$\begin{aligned} i\frac{da_{\mathrm{CW}}}{dt} &= (\omega_0 - i\gamma)a_{\mathrm{CW}} + \kappa_1 a_{\mathrm{CCW}} - it_L e^{i\phi_1}\sqrt{\kappa}S_{\mathrm{in}}, \\ i\frac{da_{\mathrm{CCW}}}{dt} &= (\omega_0 - i\gamma)a_{\mathrm{CCW}} + \kappa_2 a_{\mathrm{CW}} - it_L r_m e^{i(\phi_1+2\phi_2)}\sqrt{\kappa}S_{\mathrm{in}}, \end{aligned} \tag{7}$$

with the input signal field S_{in}. The $\kappa_1 = \alpha_1\kappa$ and $\kappa_2 = \alpha_2\kappa$ represent the unidirectional coupling coefficients, which describe the backscattering strength from the CCW (CW) mode to the CW (CCW) mode. Here $\alpha_1 = r_R(\omega_{\mathrm{CCW}})e^{2i\phi_1}$ and $\alpha_2 = r_m e^{2i\phi_2}$, where ir_R and ir_m are the field reflection coefficients at the phase-shifted FBG and the reflector, respectively. In addition, $\phi_1 = \beta L_1$ and $\phi_2 = \beta L_2$ represent the propagating phases, with β the propagation constant of the fiber and $L_{1,2}$ the propagation distance in the fiber. To better reveal the non-Hermitian character of such a system, we consider an effective Hamiltonian derived by the coupled-mode equations (7) [31],

$$H_{0,\mathrm{eff}} = \begin{bmatrix} \omega_0 - i\gamma & \alpha_1(\omega_{\mathrm{CCW}})\kappa \\ \alpha_2\kappa & \omega_0 - i\gamma \end{bmatrix}. \tag{8}$$

The necessary condition to operate the system at the EP is to generate a fully asymmetric backscattering between the counterpropagating optical modes. To satisfy this condition, the off-diagonal matrix element $\alpha_1\kappa$ needs vanish at $\Delta\omega_s = 0$, i.e., $\alpha_1(\omega_0)\kappa = 0$, while $\alpha_2\kappa$ is nonzero. Consequently, the effective non-Hermitian Hamiltonian of this photonic structure in the absence of rotation is similar to Eq. (1),

$$H_{\mathrm{ES}} = \begin{bmatrix} \omega_0 - i\gamma & 0 \\ \alpha_2\kappa & \omega_0 - i\gamma \end{bmatrix}, \tag{9}$$

where $\alpha_2\kappa$ denotes the intrinsic backscattering coefficient from the CW to CCW modes. The eigenvalues of H_{ES} are $\omega_{\mathrm{ES}1,2} = \omega_0 - i\gamma$ and the corresponding eigenvectors coalesce to one eigenvector $\tilde{a}_{\mathrm{ES}1,2} = (0, 1)^T$. Once the system was originally located at an EP in a resonance frequency ω_0, for any value of $\alpha_2\kappa$ or γ, the eigenvalues degenerate and the corresponding eigenmodes still coalesce. Accordingly, there is an EP surface consisting of these possible parameters as shown in Fig. 1(b), where the system can always be operated at an EP. This feature corresponds to prominent robustness that makes the system easier to implement in photonic technologies, because the system avoids controlling precisely the coupling coefficient and gain or loss rate of the resonator.

In Sec. II we introduced a perturbed Hamiltonian in Eq. (3) to enhance the rotation detection with a chiral EP. Consider our configuration, in which the phase-shifted grating acts as a medium that relates the rotation to the additional mode coupling. The rotation Hamiltonian is given by

$$H_{I,\mathrm{rot}} = \begin{bmatrix} \Delta\omega_s & \alpha_1(\omega_{\mathrm{CCW}})\kappa \\ 0 & -\Delta\omega_s \end{bmatrix}. \tag{10}$$

This expression, which corresponds to Eq. (3), describes the rotation inducing the mode shift and simultaneously causing a backscattering from the CCW to the CW mode generated by the phase-shifted FBG [see Fig. 1(c)]. Then the resulting eigenvalues of the non-Hermitian matrix $H = H_{\mathrm{ES}} + H_{I,\mathrm{rot}}$ are

$$\omega_{\pm} = \omega_0 - i\gamma \pm \sqrt{\kappa^2 r_R r_m e^{2i\phi} + \Delta\omega_s^2}, \tag{11}$$

where $\phi = \phi_1 + \phi_2$. Equation (11) implies that the eigenfrequencies depend on the relative phase between the counterpropagating modes [28,33]. To evaluate the sensitivity of the system, we calculate the complex eigenfrequency splitting as

$$\Delta\omega_{\mathrm{sp}} = \omega_+ - \omega_- = 2\sqrt{\kappa^2 r_R r_m e^{2i\phi} + \Delta\omega_s^2}. \tag{12}$$

The real part of $\Delta\omega_{\mathrm{sp}}$ represents the frequency splitting and the imaginary part denotes a linewidth broadening. In a small rotation, the eigenfrequency splitting $\Delta\omega_{\mathrm{sp}}$ is approximately equal to $2\sqrt{\kappa^2 r_m r_R e^{i\phi}}$. The enhancement eigenfrequency splitting provided by the EP sensor is

$$S_e = \frac{\Delta\omega_{\mathrm{sp}}}{\Delta\omega_{\mathrm{DP}}} = \frac{\sqrt{\kappa^2 r_R r_m e^{i\phi}}}{\Delta\omega_s}. \tag{13}$$

For a sufficiently low rotation rate, a larger enhancement factor can be obtained.

IV. NUMERICAL RESULTS

A. Tuning the system operating on an EP surface

As depicted in Fig. 1(a), the phase-shifted FBG is utilized to reflect the CCW mode to the CW mode and then provides the additional coupling strength, i.e., $\alpha_1\kappa$, when the system rotates. Hence, the field reflectivity r_R is related to the frequency shift $-\Delta\omega_s$ induced by the Sagnac effect. The field reflectivity and the transmissivity of the phase-shifted FBG are given by (for details see the Appendix)

$$\begin{aligned} r_R &= \left| \frac{\kappa_0\left[-\frac{n_{\mathrm{eff}}}{c}(\Delta\omega_B - \Delta\omega_s)(e^{i\varphi} - 1)r_1^2 + i\sigma r_1(1 + e^{i\varphi})\right]}{\kappa_0^2\left(1 + r_1^2 e^{i\varphi}\right) - \left[\frac{n_{\mathrm{eff}}}{c}(\Delta\omega_B - \Delta\omega_s)\right]^2\left(1 + r_1^2\right) - 2i\frac{n_{\mathrm{eff}}}{c}(\Delta\omega_B - \Delta\omega_s)\sigma r_1} \right|, \\ t_L &= \left| \frac{e^{i\varphi/2}\sigma^2 \mathrm{sech}^2(\sigma l)}{\kappa_0^2\left(1 + r_1^2 e^{i\varphi}\right) - \left(\frac{n_{\mathrm{eff}}}{c}\Delta\omega_B\right)^2\left(1 + r_1^2\right) - 2i\frac{n_{\mathrm{eff}}}{c}\Delta\omega_B\sigma r_1} \right|, \end{aligned} \tag{14}$$

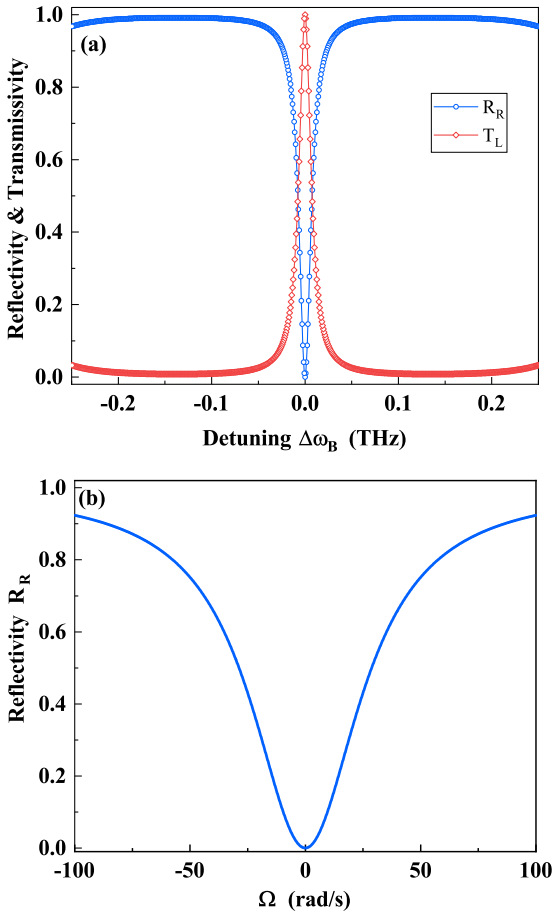

FIG. 2. (a) Reflection spectra and transmission spectra of a π-shifted FBG at $\Delta\omega_s = 0$ with an effective index $n_{\text{eff}} = 1.44$, a uniform index modulation $\Delta n_{\text{ac}} = 5 \times 10^{-4}$, a nominal period $\Lambda = 538.19$ nm, a Bragg wavelength $\lambda_B = 1550$ nm, length $l = 2$ mm, and $\Omega = 0$. (b) Reflection and transmission spectra of the π-shifted FBG as functions of the rotation rate with the system operating at an EP surface, with length $l = 8$ mm and $\Delta\omega_B = 0$.

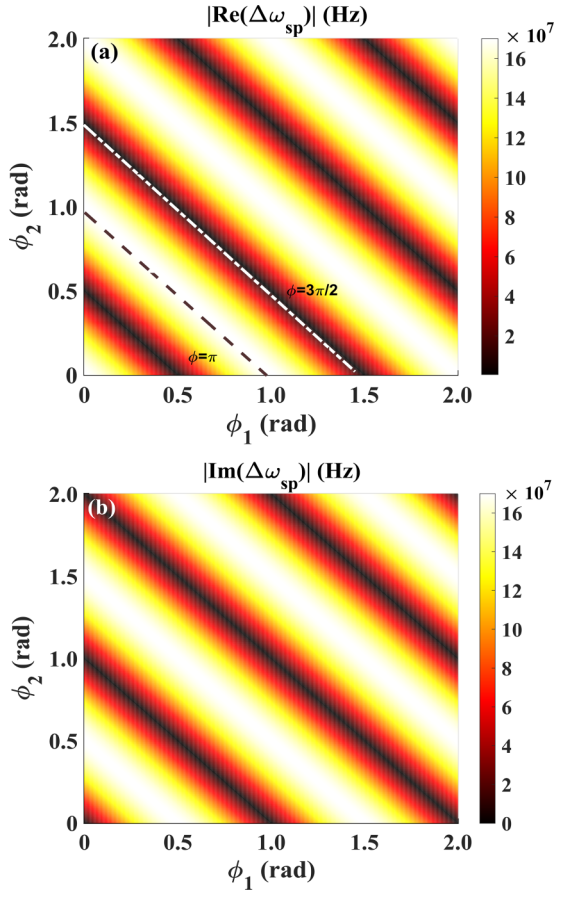

FIG. 3. Numerical simulations of the complex eigenfrequency splitting dependent on the phases ϕ_1 and ϕ_2 with rotation rate $\Omega = 5$ rad/s: (a) the real part $\text{Re}(\Delta\omega_{\text{sp}})$ of the eigenfrequency splitting and (b) the imaginary part $\text{Im}(\Delta\omega_{\text{sp}})$ of the eigenfrequency splitting. The parameters are $\kappa = 2.25 \times 10^8$ Hz, $R = 171.31$ μm, and $r_m = 0.8$.

where $\Delta\omega_B = \omega - \omega_B$, $\omega_B = 2\pi c/\lambda_B$, and ω is the frequency of the input laser. The reflectivity and transmissivity of power are $R_R = |r_R|^2$ and $T_L = |t_L|^2$, respectively. A special case of $\varphi = \pi$ corresponds to a π-shifted FBG, whose hallmark is the narrow transmission resonance in the middle of the totally reflecting band gap [34], which is important for operating the system at the EP and enhancing rotation detection.

Figure 2(a) depicts the reflection spectrum R_R and transmission spectrum T_L of the π-shifted FBG with $\Omega = 0$. A narrow peak in the transmission spectrum and a dip in the reflection spectrum of the π-shifted FBG are observed around $\Delta\omega_B = 0$. To ensure the reflectivity of the CCW mode at the FBG close to zero, the frequency of the CCW mode, i.e., ω_0 when $\Omega = 0$, should be equal to ω_B. At this time, a fully asymmetric backscattering between the counterpropagating optical modes occurs, which results in the generation of an EP surface in our system, as discussed in Sec. III. Figure 2(b) shows the reflectivity R_R as a function of the rotation rate Ω when the system operates at the EP surface. Variations in resonance frequency induced by rotation lead to changes in reflectivity, and then the additional coupling $\alpha_1\kappa$ is generated as described in Eq. (9), which breaks the degeneracy of the eigenfrequencies and pushes the system away from the EP surface.

B. Enhancement of eigenfrequency splitting

In this section, the eigenfrequency splitting of the EP surface system is numerically demonstrated. In particular, the real and imaginary parts of the complex eigenfrequency splitting at the EP can be controlled by the relative phase between the two coupling modes. In Figs. 3(a) and 3(b), the complex eigenfrequency splitting changes periodically from a minimum (maximum) to a maximum (minimum) with the variation of ϕ_1 and ϕ_2. The trends of the variations in the real and imaginary parts of the frequency splitting are the opposite. As predicted by Eq. (11), when the propagating phases in fiber are set as $\phi_1 = \pi$ and $\phi_2 = \pi$, the eigenfrequency splitting exhibits an entire real splitting $\Delta\omega_{\text{sp}} = \sqrt{\kappa^2 r_m r_R + \Delta\omega_s^2}$. Our scheme can avoid the complex eigenfrequency splitting by only adjusting appropriate propagation phases in the fiber [6].

In general, the eigenfrequency splitting induced by rotation is extracted from the transmission spectrum. According to the

input-output relation $S_{\text{out}} = t_L t_m S_{\text{in}} e^{i\phi} + a_{\text{CW}}^{\text{out}} + a_{\text{CCW}}^{\text{out}}$, with $a_{\text{CW}}^{\text{out}} = t_m\sqrt{\kappa}e^{i\phi_2}a_{\text{CW}}$ and $a_{\text{CCW}}^{\text{out}} = r_R t_m\sqrt{\kappa}e^{i(2\phi_1+\phi_2)}a_{\text{CCW}}$, the transmission coefficient is calculated by solving Eq. (7) in the steady-state approximation

$$T = \left|\frac{S_{\text{out}}}{S_{\text{in}}}\right|^2 = \left|t_m t_L\left(e^{i(\phi_1+\phi_2)} + i\kappa\frac{e^{i(\phi_1+\phi_2)}(i\mathcal{R}_2 + r_m e^{2i\phi_2}\kappa\alpha_1) + e^{i\phi'}e^{i\phi_1}r_R(ie^{2i\phi_2}r_m\mathcal{R}_1 + \kappa\alpha_2)}{\kappa^2\alpha_1\alpha_2 + \mathcal{R}_1\mathcal{R}_2}\right)\right|^2, \tag{15}$$

where $\mathcal{R}_1 = \gamma + i\Delta\omega_1$, $\mathcal{R}_2 = \gamma + i\Delta\omega_2$, $\Delta\omega_{1,2} = \Delta\omega \pm \Delta\omega_s$, $\Delta\omega = \omega_0 - \omega$ is the frequency detuning from the input laser frequency to the cavity resonance frequency, and $\phi' = 2\phi_1 + \phi_2$.

In Fig. 4 we present a series of normalized transmission spectra versus the rotation rate Ω occurring in the EP sensor and conventional gyroscope. To clearly exhibit the Sagnac-induced frequency shift in the conventional gyroscope, we plot the transmission spectra with the rotation rate $100 \times \Omega$. When the system is at rest, the transmission spectrum exhibits a resonance peak at the EP, since the resonator supports only one traveling mode that does not lead to frequency splitting. Evidently, the EP-based sensor exhibits larger frequency splitting than that of the DP-based sensor with an increase of rotation. The frequency splitting is supposed to be detected for the smaller perturbation; however, this is limited by the finite linewidths of the eigenmode that can be improved further through external gain introduced into the resonator. The parameters of the simulation in Fig. 4 are $\gamma_0 = 1.5 \times 10^7$ Hz, $\kappa = 2.25 \times 10^8$ Hz, $\gamma = 1.5 \times 10^7$ Hz, $\phi_1 = \pi$, and $\phi_2 = \pi$.

Figure 5 shows the transmission peak trajectory of the system on the contour map, which is consistent with the paths of eigenfrequencies expressed by Eq. (11). The strengths of the two resonant peaks are different, which can be explained by the superposition of the different wave components, due to the two eigenmodes containing different CCW and CW wave components.

C. Scale-factor enhancement

Considering the conventional measurement of rotation, the scale factor is generally calculated as the derivative of the eigenfrequency splitting $\Delta\omega_{\text{sp}}$ with respect to the rotation rate Ω. Hence, the Sagnac scale factor of the EP system is

$$S_{\text{ES}} = \left.\frac{\partial\Delta\omega_{\text{sp}}}{\partial\Omega}\right|_{\Omega\to 0} = \kappa\sqrt{\frac{r_m}{r_R}}\frac{\partial r_R}{\partial\Delta\omega_s}\frac{4\pi R}{n_g\lambda}, \tag{16}$$

where $4\pi R/n_g\lambda$ is the scale factor of the conventional gyroscope and $S_e = \kappa\sqrt{\frac{r_m}{r_R}}\frac{\partial r_R}{\partial\Delta\omega_s}$ is the EP enhancement factor. This enhancement factor depends on the coupling rate κ and reflection amplitude r_R that are determined by the structure parameters of the FBG. The superior performance of the EP surface-based gyroscope becomes prominent at low rotation rates, as depicted in Fig. 6, where the scale factor in the vicinity of the EP is enhanced by four orders of magnitude in comparison to the conventional Sagnac effect. The proposed EP surface system enhances the frequency splitting better than a conventional gyroscope does.

D. Noise limits

Although the EP sensor exhibits the enhancement in terms of the scale factor, it is a transduction coefficient from the rotation to the frequency splitting rather than an appropriate

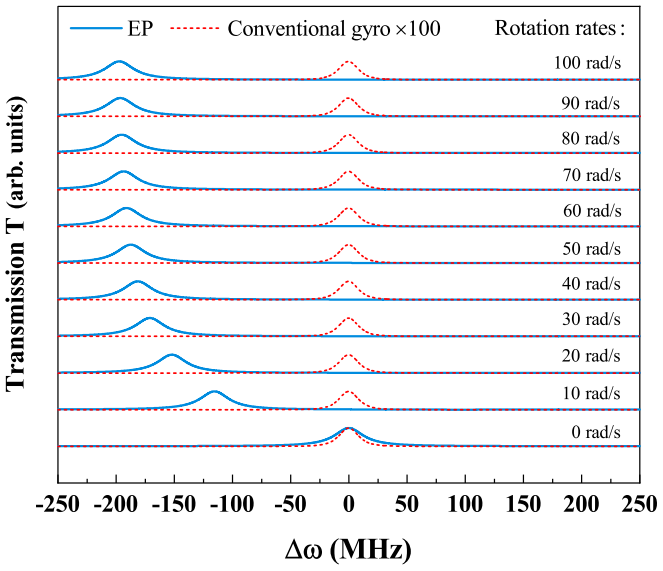

FIG. 4. Series of normalized transmission spectra of the cases of the EP sensor and conventional gyroscope as a function of rotation rate Ω. Note that the normalized transmission spectra of the conventional gyroscope are depicted with rotation rate $\Omega \times 100$.

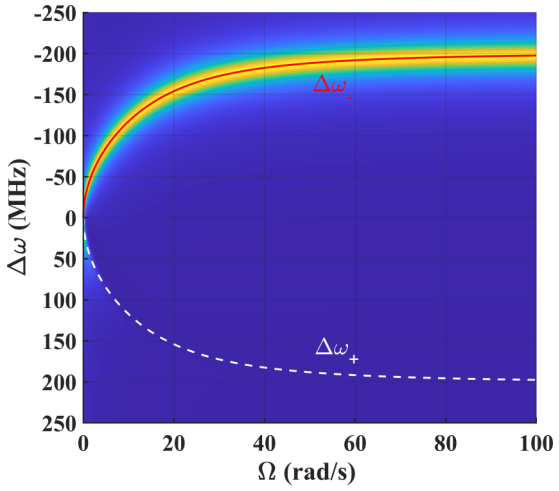

FIG. 5. Trajectory of the transmission peaks as a function of the rotation rate Ω. The red solid line and white dashed line highlight the eigenfrequencies with the variation of rotation rate Ω. Here $\Delta\omega_\pm = \omega_\pm - \omega_0$ are the eigenfrequency detunings.

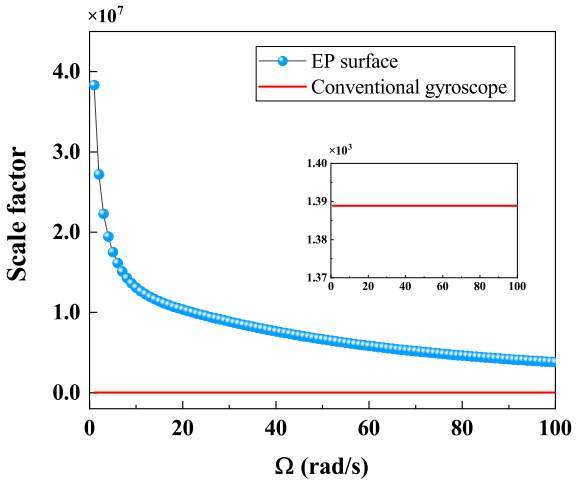

FIG. 6. Comparison of the Sagnac scale factor S_{ES} [given in Eq. (16)] of the EP surface system and the Sagnac scale factor of the conventional gyroscope. The inset shows the Sagnac scale factor of the conventional gyroscope.

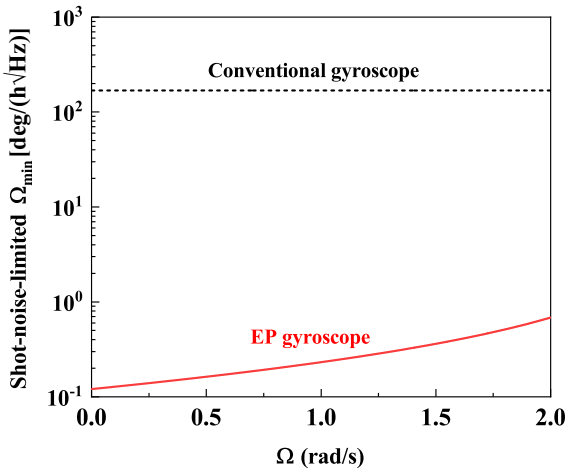

FIG. 7. Shot-noise-limited $\Omega_{\min}$ of the EP gyroscope plotted versus rotation rate. The black dashed line is the optimized shot-noise-limited $\Omega_{\min}$ of the conventional gyroscope.

metric to evaluate the detection precision. Recent works have demonstrated that the enhancement in frequency splitting at the EP does not mean an enhancement of detection precision under the noise limit [35–37]. In fact, for a conventional gyroscope, the Sagnac frequency shift can be measured with the change of transmission power when the laser is tuned to a certain frequency, which is also applicable to our system. When the gyroscope rotates, the transmission coefficient experiences a change in ΔT, which causes a transmission signal change at the detector $\Delta P_{\text{out}} = P_{\text{in}}\Delta T$ with the input power P_{in}. The sensitivity can be defined as [35]

$$S = \frac{1}{P_{\text{in}}}\left(\frac{dP_{\text{out}}}{d\Omega}\right)_{\omega}\Big|_{\Omega\to 0} = \left(\frac{dT}{d\Omega}\right)_{\omega}\Big|_{\Omega\to 0} \tag{17}$$

and is then calculated by differentiating the transmission coefficient given in Eq. (15). To evaluate the performance of the EP sensor, the most important physical quantity is the minimum detectable rotation rate under the noise limit, i.e., $\Omega_{\min} = \sigma_s/SP_{\text{in}}$, where the total noise σ_s primarily arises from the shot noise, detector noise, laser relative-intensity noise, laser-frequency noise, etc. [35]. By using the balanced-detection technique and improving the Q factor of the resonator, the noise sources can be reduced to the shot noise and detector noise, i.e.,

$$\sigma_{\text{s}} = \sqrt{\sigma_{\text{shot}}^2 + \sigma_{\text{DN}}^2} = \sqrt{2(\hbar\omega + q/\rho)P_{\text{out}} + \sigma_{\text{DN}}^2}, \tag{18}$$

where σ_{shot}^2 denotes the shot noise, σ_{DN}^2 is the detector noise, $\hbar\omega$ is the photon energy, q is the electron charge, and ρ denotes the detector responsivity. Then the minimum detectable rotation rate $\Omega_{\min}$ is written as

$$\Omega_{\min} = \frac{\sqrt{2(\hbar\omega + q/\rho)TP_{\text{in}} + \sigma_{\text{DN}}^2}}{SP_{\text{in}}}. \tag{19}$$

The detector noise is independent of the parameters of the sensor and output power. In the detector noise limit, minimizing $\Omega_{\min}$ requires maximizing the sensitivity S. In contrast, the shot noise depends on the input power and the transmission coefficient determined by the parameters of the gyroscope. When the shot noise dominates, $\Omega_{\min}$ will be minimized by optimizing the value of $\sqrt{T}/S$. Here we mainly study the shot-noise-limited minimum detectable rotation rate.

The potential of the EP sensor to enhance rotation detection can be evaluated by a comparison with the conventional gyroscope. Following the contrast principle of the gyroscopes, both the EP sensor and a single-resonator gyroscope with the same radius and intrinsic loss rate are considered. In this section, we demonstrate the passive EP sensor and passive single-resonator gyroscope. The radius of the resonator $R = 171.31$ μm and intrinsic loss rate $\gamma_0 = 1.5 \times 10^7$ Hz are chosen as discussed before. Other free parameters, namely, coupling rate κ and frequency detuning $\Delta\omega$, are optimized to minimize $\Omega_{\min}$ for the conventional gyroscope. We emphasize that the laser frequency is set at the resonance frequency of the EP sensor, because the responsivity is maximum when exciting the EP sensor on resonance, as demonstrated in Ref. [37].

Figure 7 depicts the shot-noise-limited $\Omega_{\min}$ of the EP sensor (red solid line) and the optimized shot-noise-limited $\Omega_{\min}$ of the conventional gyroscope (black dashed line). The simulated parameters are an input laser with wavelength $\lambda = 1550$ nm and input power $P_{\text{in}} = 100$ μW and the detector responsivity $\rho = 1$ A/W [35]. The shot-noise-limited $\Omega_{\min}$ of the EP sensor is approximately equal to $0.1\,\text{deg}/(\text{h}\sqrt{\text{Hz}})$ and is three orders of magnitude lower than that of a conventional gyroscope. When the system rotates and then departs from the EP, the EP sensor still has better precision than the conventional gyroscope. The reasons for the improved detection precision are as follows. For conventional gyroscopes, a rotation alters the transmission only through the Sagnac frequency shift $\Delta\omega_s$. In contrast, for the EP sensor presented here, a rotation alters the field transmission coefficient via two mechanisms: (i) the Sagnac frequency shift $\Delta\omega_s$ and (ii) the additional coupling $\alpha_1\kappa$ induced by rotation [4], as given

in Eq. (15). A rotation can introduce larger perturbation to our configuration compared to the conventional gyroscope. In addition, at an EP, having two collapsing eigenmodes makes a single transmission peak. The two eigenmodes separating from each other due to the degeneracy broken by rotation results in the reduced influence on each other; therefore, the transmission changes dramatically around the EP to generate higher sensitivity.

V. CONCLUSION

We have introduced an approach for enhancing rotation detection by using a chiral EP and proposed a non-Hermitian photonic configuration to implement it. The system can still remain at an EP when it experiences undesirable fabrication errors or experimental uncertainties. In the absence of rotation, the proposed system is finely tuned to be at the EP surface. Different from the conventional gyroscope, the phased-shifted FBG provides an additional coupling from the CCW mode to the CW mode when the system rotates. The coupling induced by rotation forces the system to depart from the EP surface, causing enhanced frequency splitting compared to the traditional Sagnac effect. The shot-noise-limited minimum detectable rotation rate is lower than that of a conventional gyroscope by three orders of magnitude. We anticipate that the EP surface system has the potential to combine robustness with sensitivity enhancement of rotation detection and is also suitable to realize an integrated photonics gyroscope in practice.

ACKNOWLEDGMENTS

We acknowledge financial support from the National Natural Science Foundation of China (Grants No. 61975005, No. 11804017, and No. 51872010) and Beijing Academy of Quantum Information Sciences (Grant No. Y18G28).

APPENDIX

In Fig. 1(a), a phase-shifted FBG relies on two uniform and symmetric FBGs with a discrete phase φ is introduced in the middle between them. For a single-mode grating, the refractive index distribution is $n(z) = n_{\text{eff}} + \Delta n_{\text{ac}} \cos[2\pi z/\Lambda + \Phi(z)]$, where n_{eff} is the effective refractive of the fiber, Δn_{ac} is the refractive modulation strength of the grating, Λ is the nominal period, z is the position along the fiber, and $\Phi(z)$ is the additional phase modulation. The input and output relation of each uniform gratings of length l ($l = L/2$) is represented by the matrix [38]

$$M_1 = M_2 = \begin{bmatrix} \cosh(\sigma l) + i\frac{\delta}{\sigma}\sinh(\sigma l) & i\frac{\kappa_0}{\sigma}\sinh(\sigma l) \\ -i\frac{\kappa_0}{\sigma}\sinh(\sigma l) & \cosh(\sigma l) - i\frac{\delta}{\sigma}\sinh(\sigma l) \end{bmatrix}, \tag{A1}$$

where $\sigma = \sqrt{\kappa_0^2 - \delta^2}$, $\kappa_0 = \Delta n_{\text{ac}}/\lambda$ is the coupling coefficient of the grating, and $\delta = 2\pi n_{\text{eff}}(\frac{1}{\lambda} - \frac{1}{\lambda_B})$ is the detuning parameter, with $\lambda_B = 2\pi n_{\text{eff}}\Lambda$ the Bragg wavelength that determines the center of the transmission and reflection.

The matrix that denotes the phase-shift region can be described as [38]

$$M_{\text{ph}} = \begin{bmatrix} e^{i\varphi/2} & 0 \\ 0 & e^{-i\varphi/2} \end{bmatrix}. \tag{A2}$$

The spectral profile from a phase-shifted FBG can be simulated using the transfer matrix method [38–41]; hence the transfer matrix F described by the phase-shifted FBG can be written as

$$F = M_2 \times M_{\text{ph}} \times M_1 = \begin{bmatrix} F_{11} & F_{12} \\ F_{21} & F_{22} \end{bmatrix}. \tag{A3}$$

Hence, the reflected amplitude and the transmission amplitude of the phase-shifted FBG can be found from the matrix F as

$$r_R = \left|\frac{F_{12}}{F_{22}}\right|, \quad t_L = \left|\frac{1}{F_{22}}\right|. \tag{A4}$$

The reflection and transmission amplitudes are calculated as

$$\begin{aligned} r_R &= \left|\frac{\kappa_0\left[-\delta(e^{i\varphi}-1)r_1^2 + i\sigma r_1(1+e^{i\varphi})\right]}{\kappa_0^2\left(1+r_1^2e^{i\varphi}\right) - \delta^2\left(1+r_1^2\right) - 2i\delta\sigma r_1}\right|, \\ t_L &= \left|\frac{e^{i\varphi/2}\sigma^2\operatorname{sech}^2(\sigma l)}{\kappa_0^2\left(1+r_1^2e^{i\varphi}\right) - \delta^2\left(1+r_1^2\right) - 2i\delta\sigma r_1}\right|, \end{aligned} \tag{A5}$$

where $r_1 = \tanh(\kappa_0 l)$. In our system, the phase-shifted FBG is utilized to reflect the CCW mode to the CW mode, that is, the reflection amplitude r_R is related to the frequency of the CCW mode. When the laser frequency is set as ω_0, the frequency detuning parameter of the CCW mode with rotation can be written as

$$\delta = 2\pi n_{\text{eff}}\left(\frac{1}{\lambda_{\text{CCW}}} - \frac{1}{\lambda_B}\right) = \frac{n_{\text{eff}}}{c}(\omega_0 - \Delta\omega_s - \omega_B). \tag{A6}$$

It should be noted that the transmission amplitude t_L is not affected by rotation and then the frequency detuning parameter in the transmission amplitude is independent of rotation. The reflectivity and transmissivity of the power are $R_R = |r_R|^2$ and $T_L = |t_L|^2$, respectively.

[1] H. Zhang, J. Y. Chen, J. J. Jin, J. Lin, L. Zhao, Z. F. Bi, A. P. Huang, and Z. S. Xiao, On-chip modulation for rotating sensing of gyroscope based on ring resonator coupled with Mach-Zehnder interferometer, Sci. Rep. **6**, 19024 (2016).

[2] W. Liang, V. S. Ilchenko, A. A. Savchenkov, E. Dale, D. Eliyahu, A. B. Matsko, and L. Maleki, Resonant microphotonic gyroscope, Optica **4**, 114 (2017).

[3] P. P. Khial, A. D. White, and A. Hajimiri, Nanophotonic optical gyroscope with reciprocal sensitivity enhancement, Nat. Photon. **12**, 671 (2018).

[4] H. Zhang, W. Li, P. Han, X. Chang, J. Liu, A. Huang, and Z. Xiao, Mode broadening induced by rotation rate in an atom assisted microresonator, J. Appl. Phys. **125**, 084502 (2019).

[5] J. Ren, H. Hodaei, G. Harari, A. U. Hassan, W. Chow, M. Soltani, D. Christodoulides, and M. Khajavikhan, Ultrasensitive micro-scale parity-time-symmetric ring laser gyroscope, Opt. Lett. **42**, 1556 (2017).

[6] M. De Carlo, F. De Leonardis, L. Lamberti, and V. M. N. Passaro, High-sensitivity real-splitting anti-PT-symmetric microscale optical gyroscope, Opt. Lett. **44**, 3956 (2019).

[7] S. Sunada, Large Sagnac frequency splitting in a ring resonator operating at an exceptional point, Phys. Rev. A **96**, 033842 (2017).

[8] M. P. Hokmabadi, A. Schumer, D. N. Christodoulides, and M. Khajavikhan, Non-Hermitian ring laser gyroscopes with enhanced sagnac sensitivity, Nature (London) **576**, 70 (2019).

[9] Y.-H. Lai, Y.-K. Lu, M.-G. Suh, Z. Yuan, and K. Vahala, Observation of the exceptional-point-enhanced Sagnac effect, Nature (London) **576**, 65 (2019).

[10] S. Jiang, X. Chang, W. Li, P. Han, Y. Zhou, H. Zhang, A. Huang, and Z. Xiao, On-chip high sensitivity rotation sensing based on higher-order exceptional points, J. Opt. Soc. Am. B **36**, 2618 (2019).

[11] L. Chang, X. Jiang, S. Hua, C. Yang, J. Wen, L. Jiang, G. Li, G. Wang, and M. Xiao, Parity-time symmetry and variable optical isolation in active-passive-coupled microresonators, Nat. Photon. **8**, 524 (2014).

[12] L. Jin, Parity-time-symmetric coupled asymmetric dimers, Phys. Rev. A **97**, 012121 (2018).

[13] L. Jin and Z. Song, Incident Direction Independent Wave Propagation and Unidirectional Lasing, Phys. Rev. Lett. **121**, 073901 (2018).

[14] A. Guo, G. J. Salamo, D. Duchesne, R. Morandotti, M. Volatier-Ravat, V. Aimez, G. A. Siviloglou, and D. N. Christodoulides, Observation of $\mathscr{P}\mathscr{T}$-Symmetry Breaking in Complex Optical Potentials, Phys. Rev. Lett. **103**, 093902 (2009).

[15] C. E. Ruter, K. G. Makris, R. El-Ganainy, D. N. Christodoulides, M. Segev, and D. Kip, Observation of parity-time symmetry in optics, Nat. Phys. **6**, 192 (2010).

[16] H. Hodaei, M. A. Miri, M. Heinrich, D. N. Christodoulides, and M. Khajavikhan, Parity-time-symmetric microring lasers, Science **346**, 975 (2014).

[17] B. Peng, Ş. K. Özdemir, F. Lei, F. Monifi, M. Gianfreda, G. L. Long, S. Fan, F. Nori, C. M. Bender, and L. Yang, Parity-time-symmetric whispering-gallery microcavities, Nat. Phys. **10**, 394 (2014).

[18] J. Schnabel, H. Cartarius, J. Main, G. Wunner, and W. D. Heiss, $\mathscr{P}\mathscr{T}$-symmetric waveguide system with evidence of a third-order exceptional point, Phys. Rev. A **95**, 053868 (2017).

[19] H. Hodaei, A. U. Hassan, S. Wittek, H. Garcia-Gracia, R. El-Ganainy, D. N. Christodoulides, and M. Khajavikhan, Enhanced sensitivity at higher-order exceptional points, Nature (London) **548**, 187 (2017).

[20] Z.-P. Liu, J. Zhang, Ş. K. Özdemir, B. Peng, H. Jing, X.-Y. Lu, C.-W. Li, L. Yang, F. Nori, and Y.-x. Liu, Metrology with $\mathscr{P}\mathscr{T}$-Symmetric Cavities: Enhanced Sensitivity near the $\mathscr{P}\mathscr{T}$-Phase Transition, Phys. Rev. Lett. **117**, 110802 (2016).

[21] F. Yang, Y.-C. Liu, and L. You, Anti-$\mathscr{P}\mathscr{T}$ symmetry in dissipatively coupled optical systems, Phys. Rev. A **96**, 053845 (2017).

[22] X.-L. Zhang and C. T. Chan, Dynamically encircling exceptional points in a three-mode waveguide system, Commun. Phys. **2**, 63 (2019).

[23] X.-L. Zhang, T. Jiang, and C. T. Chan, Dynamically encircling an exceptional point in anti-parity-time symmetric systems: Asymmetric mode switching for symmetry-broken modes, Light: Sci. Appl. **8**, 88 (2019).

[24] M. De Carlo, Exceptional points of parity-time- and anti-parity-time-symmetric devices for refractive index and absorption-based sensing, Results Opt. **2**, 100052 (2021).

[25] Q. Zhong, S. K. Ozdemir, A. Eisfeld, A. Metelmann, and R. El-Ganainy, Exceptional-Point-Based Optical Amplifiers, Phys. Rev. Appl. **13**, 014070 (2020).

[26] J. Wiersig, Enhancing the Sensitivity of Frequency and Energy Splitting Detection by using Exceptional Points: Application to Microcavity Sensors for Single-Particle Detection, Phys. Rev. Lett. **112**, 203901 (2014).

[27] J. Wiersig, Sensors operating at exceptional points: General theory, Phys. Rev. A **93**, 033809 (2016).

[28] C. Wang, X. Jiang, G. Zhao, M. Zhang, C. W. Hsu, B. Peng, A. D. Stone, L. Jiang, and L. Yang, Electromagnetically induced transparency at a chiral exceptional point, Nat. Phys. **16**, 334 (2020).

[29] W. Chen, Ş. K. Özdemir, G. Zhao, J. Wiersig, and L. Yang, Exceptional points enhance sensing in an optical microcavity, Nature (London) **548**, 192 (2017).

[30] Q. Zhong, S. Nelson, Ş. K. Özdemir, and R. El-Ganainy, Controlling directional absorption with chiral exceptional surfaces, Opt. Lett. **44**, 5242 (2019).

[31] Q. Zhong, J. Ren, M. Khajavikhan, D. N. Christodoulides, Ş. K. Özdemir, and R. El-Ganainy, Sensing with Exceptional Surfaces in Order to Combine Sensitivity with Robustness, Phys. Rev. Lett. **122**, 153902 (2019).

[32] J. Zhu, S. K. Ozdemir, Y.-F. Xiao, L. Li, L. He, D.-R. Chen, and L. Yang, On-chip single nanoparticle detection and sizing by mode splitting in an ultrahigh-Q microresonator, Nat. Photon. **4**, 46 (2010).

[33] G.-Q. Qin, R.-R. Xie, H. Zhang, Y.-Q. Hu, M. Wang, G.-Q. Li, H. Xu, F. Lei, D. Ruan, and G.-L. Long, Experimental realization of sensitivity enhancement and suppression with exceptional surfaces, Laser Photon. Rev. **15**, 2000569 (2021).

[34] G. Skolianos, A. Arora, M. Bernier, and M. Digonnet, Slow light in fiber Bragg gratings and its applications, J. Phys. D **49**, 463001 (2016).

[35] M. J. Grant and M. J. Digonnet, Rotation sensitivity and shot-noise-limited detection in an exceptional-point coupled-ring gyroscope, Opt. Lett. **46**, 2936 (2021).

[36] M. J. Grant and M. J. Digonnet, Enhanced rotation sensing and exceptional points in a parity-time-symmetric coupled-ring gyroscope, Opt. Lett. **45**, 6538 (2020).

[37] W. Langbein, No exceptional precision of exceptional-point sensors, Phys. Rev. A **98**, 023805 (2018).

[38] S. V. Raja, A. Govindarajan, A. Mahalingam, and M. Lakshmanan, Phase-shifted $\mathscr{P}\mathscr{T}$-symmetric periodic structures, Phys. Rev. A **102**, 013515 (2020).

[39] T. Erdogan, Fiber grating spectra, J. Lightw. Technol. **15**, 1277 (1997).

[40] L. Wei and J. W. Y. Lit, Phase-shifted Bragg grating filters with symmetrical structures, J. Lightw. Technol. **15**, 1405 (1997).

[41] X. Liu, X. Shu, and H. Cao, Proposal of a phase-shift fiber Bragg grating as an optical differentiator and an optical integrator simultaneously, IEEE Photon. J. **10**, 7800907 (2018).